NANO LETTERS

Letter

pubs.acs.org/NanoLett

Orientation-Dependent Interfacial Mobility Governs the Anisotropic Swelling in Lithiated Silicon Nanowires

Hui Yang,[†] Shan Huang,[‡] Xu Huang,[†] Feifei Fan,[‡] Wentao Liang,[†,§] Xiao Hua Liu,[§] Long-Qing Chen,[∥] Jian Yu Huang,[§] Ju Li,*[,⊥] Ting Zhu,*[,‡] and Sulin Zhang*[,†]

[†]Department of Engineering Science and Mechanics and [∥]Department of Materials Science and Engineering, Pennsylvania State University, University Park, Pennsylvania 16802, United States

[‡]Woodruff School of Mechanical Engineering, Georgia Institute of Technology, Atlanta, Georgia 30332, United States

[§]Center for Integrated Nanotechnologies, Sandia National Laboratories, Albuquerque, New Mexico 87185, United States

[⊥]Department of Nuclear Science and Engineering and Department of Materials Science and Engineering, Massachusetts Institute of Technology, Cambridge, Massachusetts 02139, United States

ABSTRACT: Recent independent experiments demonstrated that the lithiation-induced volume expansion in silicon nanowires, nanopillars, and microslabs is highly anisotropic, with predominant expansion along the ⟨110⟩ direction but negligibly small expansion along the ⟨111⟩ direction. The origin of such anisotropic behavior remains elusive. Here, we develop a chemomechanical model to study the phase evolution and morphological changes in lithiated silicon nanowires. The model couples the diffusive reaction of lithium with the lithiation-induced elasto-plastic deformation. We show that the apparent anisotropic swelling is critically controlled by the orientation-dependent mobility of the core−shell interface, i.e., the lithiation reaction rate at the atomically sharp phase boundary between the crystalline core and the amorphous shell. Our results also underscore the importance of structural relaxation by plastic flow behind the moving phase boundary, which is essential to quantitative prediction of the experimentally observed morphologies of lithiated silicon nanowires. The study sheds light on the lithiation-mediated failure in nanowire-based electrodes, and the modeling framework provides a basis for simulating the morphological evolution, stress generation, and fracture in high-capacity electrodes for the next-generation lithium-ion batteries.

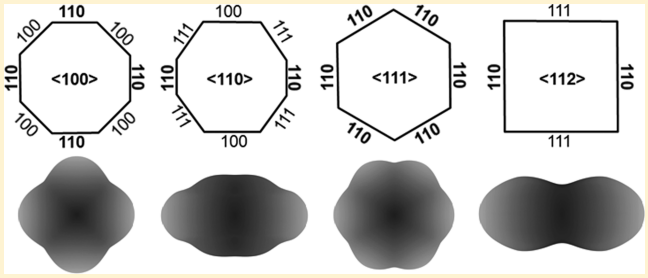

KEYWORDS: *Silicon nanowire, lithium-ion battery, anisotropic swelling, orientation-dependent interfacial mobility, diffusion, elasto-plastic deformation*

The demand for high-capacity lithium-ion batteries (LIBs) for portable electronics, hybrid electric vehicles, and large scale energy storage has stimulated the relentless search for new electrode materials.[1−3] Silicon is being considered as one of the leading candidates to replace current carbonaceous anodes in LIBs for its high theoretical capacity.[4−8] However, rapid, irreversible capacity decay and poor cyclability, which arise largely due to the huge volume changes (∼300%) induced by Li insertion and extraction, remain a major technical barrier for commercializing high-capacity anodes, such as Si.[9−13] It has been widely believed that nanoscale materials can facilitate strain relaxation, enhance flaw tolerance, shorten lithium ion and electron diffusion paths, and increase surface area of the electrodes to better react with Li.[14,15] Scaling the size of electrode materials down to the nanometer range thus represents one of the promising means to mitigate the adverse effects for better capacity retention.[5,16−20] Despite impressive transmission electron microscopy (TEM) studies on the electrochemical lithiation of the nanostructured Si anodes in the past few years,[5,8,10,11,18,20−26] their deformation and failure mechanisms are still not yet well understood.

Recent in situ experimental studies showed that the lithiated silicon nanowires (SiNWs) not only undergo large volume expansion[8] but also swell in an anisotropic manner.[23,24] For example, in a fully lithiated ⟨112⟩-oriented SiNW, the expansion along the [110] direction (∼170%) is about nine times that along the [111] direction (∼20%) within the cross section.[23] The large deformation anisotropy can neither be explained by the marginal anisotropy in the elastic properties of Si crystals nor by the diffusion anisotropy since diffusivity is isotropic in cubic crystals of Si.[27] Clearly, the chemomechanical mechanism governing the anisotropic swelling in lithiated Si warrants further study for a mechanistic understanding of deformation and fracture in nanostructured Si-based electrodes. Recent experiments evidenced that lithiation in crystalline Si (c-

Received: December 15, 2011
Revised: March 20, 2012

   dx.doi.org/10.1021/nl204437t | *Nano Lett.* XXXX, XXX, XXX−XXX

Si) proceeds by the movement of an atomically sharp reaction front that separates the c-Si with the amorphous product of Li_xSi alloy.[8,23,28] Inspired by the previous study of interface-controlled diffusive reactions[29−31] and first-principles calculations,[32] we hypothesize that the mobility of the lithiation interface depends on the local crystallographic orientation of exposed c-Si surface. To test this hypothesis, we develop a chemomechanical model that couples the diffusive reaction of Li with elasto-plastic deformation to simulate the lithiation-induced morphological changes in SiNWs. Our model predicts the anisotropic swelling of lithiated SiNWs with various axial orientations, which closely agrees with the experiments. Our mechanics analyses also provide insight into the failure mechanisms of Si anodes.

During electrochemical lithiation, Li diffuses within and reacts with Si at room temperature. A characteristic feature of this electrochemical process is the formation of a phase boundary,[8,23,28] which separates the lithiated product and pristine Si crystal (Figure 1). Recent TEM studies revealed that

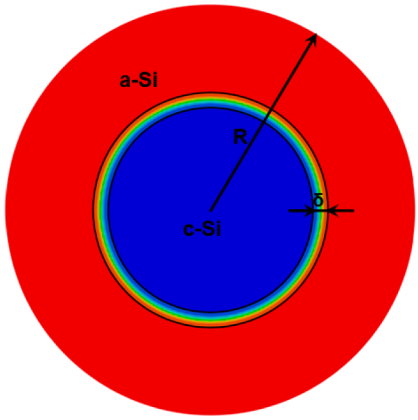

Figure 1. Electrochemical lithiation results in an atomically sharp phase boundary (as represented by a thin ring bound in between the two solid black circles) that separates nearly fully lithiated amorphous silicon (a-Si) phase (red region) and crystalline silicon (c-Si) phase (blue region).

such phase boundary is atomically sharp, with a width on the order of 1 nm.[28] The sharpness appears to be independent of the specimen size and the lithiation rate. The lithiated phase likely consists of amorphous $Li_{3.75}Si$, evidenced by the apparent volume expansion close to that of crystalline $Li_{3.75}Si$ as well as the dynamic formation of $Li_{3.75}Si$ nanocrystals within the amorphous phase.[23] Within the c-Si core, the Li concentration appears to be low, evidenced by the intact lattice structure with the measured lattice spacing close to that of a perfect c-Si.[8,23] The lithiation reaction front is therefore identified as a phase boundary, across which there is an abrupt change of Li concentration. Namely, the Li-poor and -rich phases do not transform continuously into each other with changing composition, and lithiation is mediated by the phase boundary migration. We thus develop a two-phase model, in contrast to the single-phase one in which the Li concentration gradually varies in Si.[33] The two- and single-phase models yield large differences in the lithiation-induced stress profiles and predict different fracture initiation locations (outer surface for the former vs core for the latter) of lithiated Si nanoparticles. Interested readers may refer to a recent accompanying manuscript for detailed discussions of this aspect.[34]

The relative time scale of Li diffusion and Li−Si reaction is another key factor of the lithiation process. Physically, the lithiation involves two processes in series: (1) the Li diffusion through the lithiated shell and (2) the chemical reaction at the phase boundary. The characteristic time of long-range Li diffusion scales with $\tau_D \sim L^2/D$,[14] where L and D are the lithiated shell thickness and Li diffusivity in Si, respectively. On the other hand, the Li−Si reaction is a short-range process involving the disruption of the c-Si lattice and the formation of the amorphous lithiated product at the reaction front. The characteristic time scale τ_R of lithiation associated with such interface-controlled reaction is L/k, where k is the reaction rate constant. For nanometer-sized specimens, $\tau_D \ll \tau_R$ usually holds. As a result, the reaction front propagates much slower than the diffusion of Li behind it, and lithiation is limited by the reaction rate. On the contrary, for large-sized specimens, $\tau_D \gg \tau_R$ is usually satisfied, and lithiation is diffusion controlled. A transition between the two regimes exists at an intermediate thickness L.

The origin of lithiation anisotropy warrants further discussion. Lithium diffusion in Si is isotropic in both amorphous and crystalline states. In front of the reaction front, Si remains crystalline but undergoes elastic deformation arising from the lithiation-induced strain mismatch. It may be argued that the anisotropic elastic properties of c-Si could lead to stress anisotropy, which in turn causes anisotropic diffusion near the reaction front. Despite a seemingly valid argument, the marginal anisotropy of elastic properties (elastic moduli differ by only ~10% in ⟨111⟩ and ⟨110⟩ directions)[35] is unlikely to account for the huge anisotropy of expansions in lithiated SiNWs (swelling in ⟨110⟩ is about nine times that in ⟨111⟩). In addition, the inconsistency in the order of anisotropy (with elastic moduli $E_{\langle 111\rangle} > E_{\langle 110\rangle} > E_{\langle 100\rangle}$ versus lithiation-induced expansion $\varepsilon_{\langle 110\rangle} > \varepsilon_{\langle 100\rangle} > \varepsilon_{\langle 111\rangle}$) further excludes the possibility of the dominant role of elastic anisotropy. Here we propose that the primary source of anisotropic swelling should stem from the crystallographic orientation dependence of the lithiation rate at the sharp reaction front, i.e., phase boundary. As a matter of fact, such orientation dependence of interfacial reactions has been proposed and reported in the study of solid-state reactions of crystals.[31,36−38]

Based on the above considerations, we next describe a chemomechanical model for simulating the phase evolution and morphological changes in lithiated SiNWs. As discussed earlier, the lithiation involves two processes in series: (1) the Li diffusion through the lithiated shell and (2) the chemical reaction at the phase boundary. To simulate these two concurrent processes, we describe Li transport in Si by the classic diffusion equation in the entire domain, $\partial c/\partial t = \nabla\cdot(D\nabla c)$, where ∇ represents the vector differential operator with respect to spatial coordinates and c the lithium concentration. The orientation-dependent reaction rate or interfacial mobility is modeled by the anisotropic interfacial diffusion across an interfacial domain between the lithiated and unlithiated regions, as detailed next.

To produce a sharp phase boundary, we set Li diffusivity to be concentration dependent: $D = D_0[1/(1-c) - 2\alpha c]$, where D_0 is a diffusion constant and α is a tunable constant to control the concentration profile near the phase boundary.[23] Note that the Li concentration is normalized by that of the fully lithiated phase of $Li_{3.75}Si$; namely, $c = 1$ represents $Li_{3.75}Si$, while $c = 0$ pure Si. This concentration-dependent diffusivity becomes considerably large in the lithiated shell ($c \approx 1$) and negligibly

dx.doi.org/10.1021/nl204437t | Nano Lett. XXXX, XXX, XXX−XXX

small near the unlithiated core ($c \approx 0$). It well captures the interfacial reaction as a rate-controlling step and facilitates the formation of the Li-poor core and the Li-rich shell with a moving phase boundary in between, as observed in the experiments.[23] To simulate the evolution of such a core−shell structure, the above nonlinear diffusion model is implemented in the finite element package ABAQUS. Here we note that unlike the phase field model,[39] our nonlinear diffusion model does not contain a material length scale related to the interface thickness. Instead, we introduce an interfacial domain with a finite thickness, as to be detailed next.

In order to study the effects of orientation-dependent interfacial mobility, we have divided the system into three domains: a bulk domain (where $c \geq c_+$) behind the reaction front, another bulk domain (where $c < c_-$) in front of the reaction front, and an interfacial domain (where $c_- < c < c_+$). Here c_+ is assigned to be close to 1 while c_- to 0. Within the two bulk domains, the aforementioned nonlinear, isotropic diffusivity is used. In contrast, the "diffusivity" within the interfacial domain is assumed to depend on the local crystallographic orientation of exposed c-Si surface, whose surface normal is determined by the orientation of the largest local concentration gradient. It should be emphasized that lithium transport in the interfacial domain occurs through chemical reactions that are characterized by the disruption of the c-Si lattice and production of the amorphous $Li_{3.75}Si$ and thus expected to differ drastically from the atomic processes of Li diffusion in the two bulk domains. This interfacial reaction is here treated by diffusion across the interface for numerical convenience. Compared to the two bulk domains, the interfacial domain is considerably narrow, spanning a few elements in finite element simulations. When it is idealized as a mathematical interface with zero thickness, our three-domain model is reduced to the conventional two-domain model. It follows that the orientation dependence of flux in the interfacial domain leads to interfacial mobility anisotropy, since the Li flux J can be related to the interfacial velocity v by $J = v/\Omega$, where Ω is the volume of the Li−Si alloy formed per Li.

Currently, there are no available experimental and atomistic data of interfacial mobilities. We fit the orientation-dependent interfacial diffusion constants by best matching the simulated morphologies with experimental observations, i.e., $D^F_{0,\langle 110\rangle} \approx 6D^F_{0,\langle 100\rangle} \approx 60D^F_{0,\langle 111\rangle}$, where the associated orientations are indicated in the subscripts and the superscript "F" indicates the rate constant at the reaction front. Notice that such orientation-dependent interfacial diffusivities effectively play the same role of orientation-dependent reaction rate constants when the interfacial layer is regarded approximately as a sharp interface, as discussed above. The parametric settings of those diffusivities (reaction rates) are consistent with recent experimental observations that the phase boundary migrates much faster along $\langle 110\rangle$ than other directions, while slowest along $\langle 111\rangle$.[13,23,24] A smooth interpolation from the above diffusion constants gives those of other directions. We also set the diffusion constant in the amorphous domain as $D^B_0 = D^F_{0,\langle 100\rangle}$, where the superscript "B" denotes parameters in the two bulk domains. It should be noted that due to the high Li concentration and relatively large diffusion constant in the amorphous region, the diffusivity D is much larger in the amorphous region than that at the reaction front. This effectively realizes the two-phase microstructure with a sharp phase boundary whose movement is rate-limiting.

In experiments Li was observed to quickly cover the outer surface of SiNWs or Si nanoparticles due to its much lower migration barriers on the Si surface than in the bulk.[8,23,40] We thus prescribe a Dirichlet boundary condition that assumes saturated Li concentration on the SiNW outer surface ($c = 1$) throughout the lithiation process. At any given time, the narrow interfacial domain ($c_- < c < c_+$) is identified based on the current lithium concentration profile. At any point within such an interfacial domain, the local interfacial orientation is determined from the direction of the largest Li concentration gradient, i.e., that of the resultant concentration gradient vector. The diffusion constant can be calculated from the interpolated function of the orientation-dependent diffusion constant, as discussed earlier. The Li concentration profile is then updated to simulate the migration of the phase boundary, i.e., the radially inward movement of the core−shell interface.

Lithium insertion induces chemical strains that further cause elastic−plastic strains. During lithiation, a core−shell structure develops in SiNWs.[23,28] At the sharp core−shell interface, the abrupt change of Li concentration causes large chemical strains; the lithiated shell behind the reaction front undergoes the structural relaxation by plastic flow;[41] and the crystalline core deforms elastically. We adopt an isotropic elastic and perfectly plastic model to describe the lithiation-induced deformation. The strain rate $\dot{\varepsilon}_{ij}$ is composed of three contributions: $\dot{\varepsilon}_{ij} = \dot{\varepsilon}^c_{ij} + \dot{\varepsilon}^e_{ij} + \dot{\varepsilon}^p_{ij}$,[33] where both i and j run from 1 to 3 for three-dimensional (3D) problems (from 1 to 2 for 2D case), representing the three Cartesian coordinates. Here the lithiation-induced electrochemical strain rate $\dot{\varepsilon}^c_{ij}$ is assumed to be dilational and proportional to the increment of the lithium concentration, $\dot{\varepsilon}^c_{ij} = \beta\delta_{ij}\dot{c}$, where $\beta = 0.6$ represents the lithiation expansion coefficient, and δ_{ij} is the Kronecker delta ($\delta_{ij} = 1$ for $i = j$ and $\delta_{ij} = 0$ otherwise). Assuming that Si is isotropic in the elastic regime, the increment of the elastic strain, $\dot{\varepsilon}^e_{ij}$, obeys Hooke's law with two elastic constants, i.e., Young's modulus E and Poisson's ratio ν. The Young's modulus and Poisson's ratio are both assumed to linearly vary with Li concentration from 160 to 40 GPa and from 0.24 to 0.22,[35,42,43] respectively. The increment of the plastic strain, $\dot{\varepsilon}^p_{ij}$, obeys the classic J_2-flow rule. Namely, plastic yielding occurs when the equivalent stress, $\sigma_{eq} = (3s_{ij}s_{ij}/2)^{1/2}$, equals the yield strength, σ_Y. Here $s_{ij} = \sigma_{ij} - \sigma_{kk}\delta_{ij}/3$ is the deviatoric stress, where σ_{ij} is the Cauchy stress and repeated indices mean summation. Note that $\dot{\varepsilon}^p_{ij}$ is proportional to s_{ij} and can be determined by solving the boundary value problem $\dot{\sigma}_{ij,j} = 0$ with a traction-free boundary condition. We set the yield stress σ_Y to be 1.5 GPa, consistent with the previously reported experimental data.[28,41,44] For such a low yield stress, the simulation geometry needs to be carefully meshed to ensure numerical stability and convergence.

We next apply the coupled chemomechanical model to simulate the morphological changes of the SiNWs during electrochemical lithiation. Four different axial orientations of $\langle 100\rangle$, $\langle 110\rangle$, $\langle 111\rangle$, and $\langle 112\rangle$ are considered.[23,24] The characteristic crystallographic orientations in respective cross sections are shown in Figure 2. While the model is generally applicable to 3D cases, we here simplify the problem to the plane−strain condition, considering that the axial elongation is much less than the cross-sectional expansion in lithiated SiNWs.[23] Prior to lithiation, the cross sections of the SiNWs in all cases are circular with radius R. The length and time-related variables are normalized by R and the time required to fully lithiate the cross section, respectively. The circular cross section is discretized by finite element meshes. The mesh size is

dx.doi.org/10.1021/nl204437t | Nano Lett. XXXX, XXX, XXX−XXX

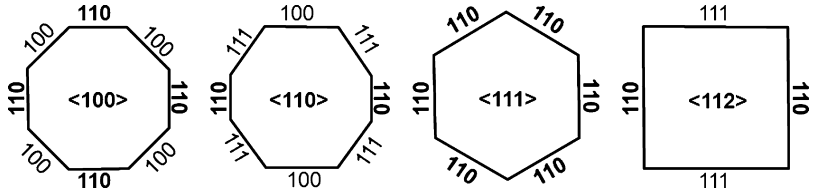

Figure 2. The characteristic crystallographic orientations of the SiNWs, where the indices at the center represent the axial orientations of each wire and other indices the normal orientations of the facets.

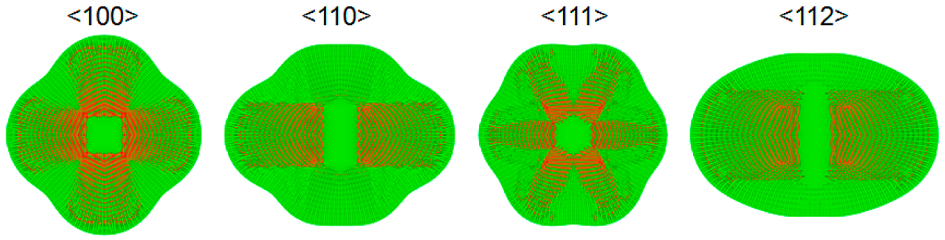

Figure 3. Lithium flux profiles at a representative lithiation snapshot (t = 0.4) for all the four SiNWs, showing that the dominant flux in the ⟨110⟩ directions, a direct consequence of high reactivity of Li at the {110} phase boundary.

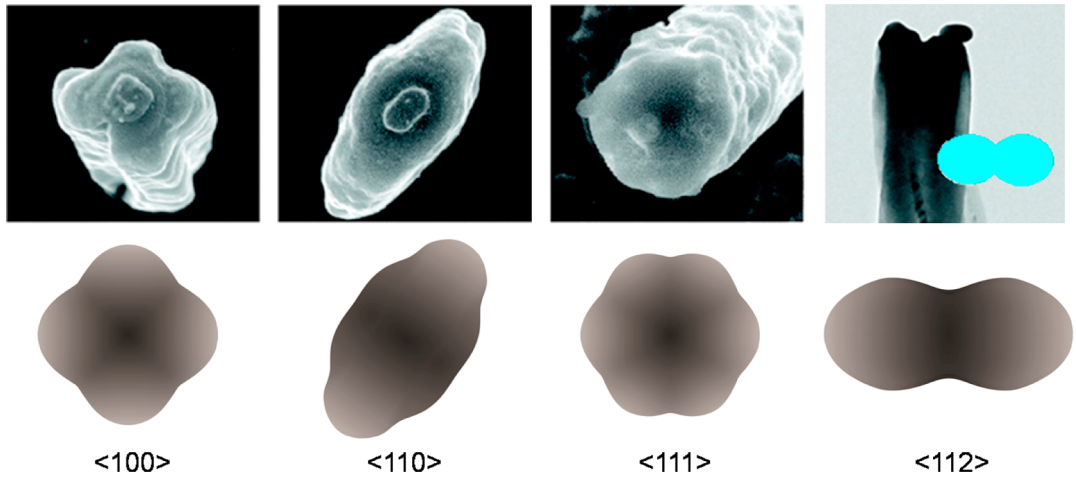

Figure 4. Comparison between experiment[23,24] (top) and our modeling (bottom) in terms of the cross-sectional morphologies of fully lithiated SiNWs with different axial orientations.

sufficiently small, such that the narrow interfacial domain can still accommodate a few elements. At any time t ($0 < t < 1$), the Li concentration profile is computed by solving the diffusion equation. The concentration profile is then fed into the mechanics model to obtain the strain and stress distributions in lithiated SiNWs.

Before presenting the main results, we first show that the Li reaction-diffusion model effectively captures the essential features of Li transport. Figure 3 plots the Li flux profile at time t = 0.4, where the flux vectors are represented by red arrowed lines (the arrow represents the direction of the flux, while the length of the arrowed lines the magnitude). The resulting flux patterns indicate that the Li diffusion in the ⟨110⟩ directions is considerably faster than other directions in the lithiated shell, despite the imposed isotropic diffusivity in the lithiated shell. Such ⟨110⟩-preferred flux patterns result from the large reaction rate at the {110} phase boundary, i.e., the high mobility of the {110} core−shell interface. Our results also yield the sharp phase boundary, as will be demonstrated later.

Figure 4 shows the fully lithiated cross-sectional morphologies of the four SiNWs, which agree closely with the experiments.[23,24] The deformation anisotropy is measured by the ratio of the deformed length in the maximal expansion direction to that in the minimal expansion direction. The simulated deformation anisotropies are 1.24, 1.80, 1.12, and 2.28 for the ⟨100⟩, ⟨110⟩, ⟨111⟩, and ⟨112⟩ SiNWs, respectively, which compare to 1.23, 1.68, 1.05, and 2.25 in the previous experiments.[23,24]

We next examine the stress evolution in the cross section of SiNWs. According to our simulation results, the primary features of stress generation in all the four SiNWs are qualitatively similar. For the convenience of discussion we present the history of stresses experienced by a representative material point, located at r = 0.55R along the maximal radial expansion direction of the ⟨112⟩ SiNW in the pristine state. Figure 5 plots the evolution of the equivalent and hydrostatic stresses (dashed and solid blue lines, respectively), along with that of the Li concentration at the point (red line). One notices that the reaction front reaches the material point at time t = 0.1, when the Li concentration begins to rise, followed by an abrupt increase at $t \approx 0.2$. The reaction front completely sweeps across this material point at t = 0.3, beyond which it becomes fully lithiated. During the sweeping process, the equivalent stress at this material point rapidly jumps to the yield stress and

dx.doi.org/10.1021/nl204437t | Nano Lett. XXXX, XXX, XXX−XXX

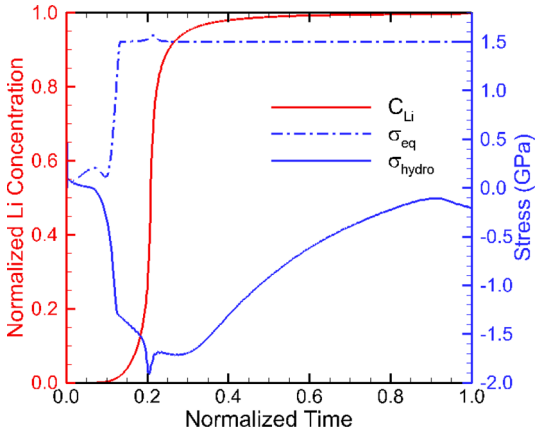

Figure 5. Stress evolution of a representative material point ($r = 0.55R$ in the pristine state) in the ⟨112⟩-oriented SiNW as the reaction front sweeps through it. The variation of Li concentration at the same point indicates the lithiation stage.

maintains approximately on that level as lithiation further proceeds. In contrast, the point is subjected to hydrostatic tension when located in the crystalline core, but hydrostatic compression once it is swept by the reaction front and beyond. The hydrostatic compression reaches the maximum when the point is roughly located at the center of the reaction front. The high hydrostatic compression may play an important role in reducing the reaction rate at the reaction front and the diffusivity behind it. Such effects are not taken into account in the current model.

To provide insight into the initiation of fracture in lithiated Si, Figure 6 plots the maximal in-plane principal stress (b1 and b2), along with Li concentration profiles (a1 and a2), for the ⟨100⟩ and ⟨112⟩ SiNWs at four different lithiation snapshots t = 0.01, 0.05, 0.10, and 0.30 from top to bottom. Results for the other two SiNWs are qualitatively similar and not shown here.

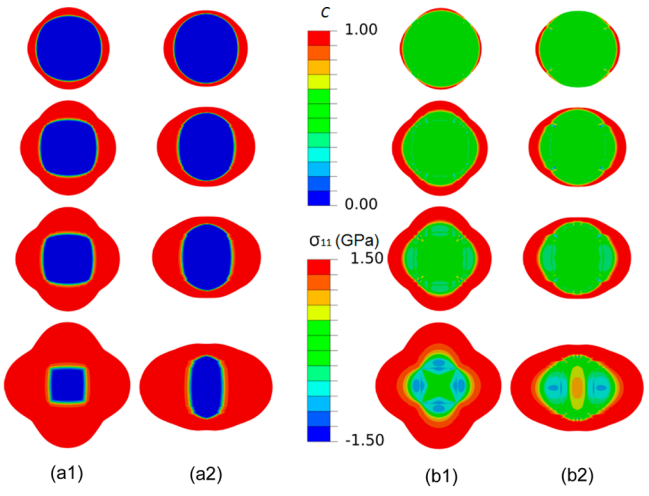

Figure 6. The maximal in-plane principal stress in the cross sections of the ⟨100⟩ (b1) and ⟨112⟩ (b2) SiNWs at four lithiation snapshots. The corresponding lithiation states are shown in (a1) and (a2). The maximal in-plane principal stress is always tensile in the lithiated shell and compressive around the reaction front. However, it changes from tension to compression in the unlithiated core at a late stage of lithiation, when the unlithiated crystalline core is small. The maximal tensile stress occurs at the outer surface of SiNWs, suggesting the location at which fracture first initiates.

The reaction fronts at each snapshot can be identified by the sharp change of Li concentrations as well as the boundary across which the maximal in-plane principal stress changes its sign. For both cases, the maximal in-plane principal stress is always tensile in the fully lithiated shell and compressive around the reaction front. However, it changes from tension to compression in the unlithiated crystalline core at a late stage of lithiation when the unlithiated core is small. We further notice that the maximal tensile stress occurs at the outer surfaces exclusively for all the SiNWs and could be even larger than σ_Y, which often occurs for the elastic−plastic deformation subjected to multiaxial stresses. Such a high tensile stress may well exceed the fracture strength of the amorphous lithiated silicon. As a result, facture may initiate from the outer surface in the lithiated SiNWs. For instance, for the ⟨112⟩ SiNW, the maximal in-plane tensile stress occurs at the outer surface along the vertical axis, which well explains the self-splitting of a single SiNW into two subwires observed in experiment.[23] It should be pointed out that the result of hoop tension in the surface layer is opposite to that from the single-phase model, which predicts that fracture instead initiates at the unlithiated crystalline core.

In summary, we have developed a chemomechanical model that couples the diffusive reaction of Li with Li insertion induced elasto-plastic deformation in lithiated Si. Our analysis demonstrated that the origin of anisotropic swelling in lithiated SiNWs can be attributed to the crystallographic orientation-dependent reaction rate at the interface between the amorphous shell of $Li_{3.75}Si$ and crystalline core of Si. As a direct consequence of the orientation-dependent interfacial mobilities, our model faithfully reproduces the cross-sectional morphologies of lithiated SiNWs of different axial orientations observed in previous experiments. In addition, to achieve such good agreement, we found it is essential to account for the structural relaxation by plastic deformation in the lithiated phase. Our stress analysis also revealed the evolution of hydrostatic stresses, which could play a critical role in reducing Li diffusion and reaction rates. Moreover, our model predicts that the maximal in-plane principal tensile stress always occurs at the outer surface, where fracture is predicted to first initiate, consistent with previous experimental observations. In-situ high-resolution TEM studies on the atomistic origin of the orientation-dependent interfacial mobility are currently underway, and a separate manuscript is being developed to report the experimental findings.

It should be pointed out that our modeling results are obtained on the basis of both the relative reaction rates for different crystallographic directions and the reaction rate relative to the diffusion time scale. Essentially, the deformation morphologies and stress profiles remain the same as long as these relative rates remain unchanged, independent of the absolute lithiation rates. This is because the relative rates (not the absolute rates) determine the geometry of the reaction front, which further determines the stress developed in the lithiated/unlithiated Si as well as the resulting anisotropic morphologies. However, the relative rates could be modified by the applied electrical field. With modified relative rates, both the deformation morphologies and stress distribution would be subjected to changes.

We conclude by emphasizing that the orientation-dependent reaction rates at the atomically sharp phase boundary, along with structural relaxation by large plastic flow, are the key features in our modeling framework in order to fully account for the deformation mechanics of lithiated Si. It should also be

dx.doi.org/10.1021/nl204437t | Nano Lett. XXXX, XXX, XXX−XXX

noted that the present model couples Li transport with deformation mechanics in a unidirectional manner. In the future, we will extend the model to bidirectional coupling by incorporating the possible stress dependence of the diffusion and reaction rates. Such framework is expected to be applicable to other high-capacity anode materials. The mechanistic understanding of morphological evolution and stress generation in these materials is essential to enable the rational design of next-generation failure resistant electrodes.

AUTHOR INFORMATION

Corresponding Author

*E-mail: suz10@psu.edu; ting.zhu@me.gatech.edu; liju@mit.edu

Notes

The authors declare no competing financial interest.

ACKNOWLEDGMENTS

S.Z. acknowledges support by NSF grant CMMI-0900692. T.Z. acknowledges support by NSF grants CMMI-0758554 and 1100205. J.Y.H. acknowledges the support from the Center for Integrated Nanotechnologies at Sandia National Lab, a U.S. Department of Energy, Office of Basic Energy Sciences user facility. Sandia National Laboratories is a multiprogram laboratory managed and operated by Sandia Corporation, a wholly owned subsidiary of Lockheed Martin Company, for the U.S. Department of Energy's National Nuclear Security Administration under Contract DE-AC04- 94AL85000. L.-Q.C. acknowledges the support by NSF grant numbers DMR 0710483 and 1006541. J.L. acknowledges the support by NSF DMR-1008104 and DMR-1120901 and AFOSR FA9550-08-1-0325.

REFERENCES

(1) Tarascon, J. M.; Armand, M. *Nature* **2001**, *414* (6861), 359−367.
(2) Arico, A. S.; Bruce, P.; Scrosati, B.; Tarascon, J.-M.; van Schalkwijk, W. *Nat. Mater.* **2005**, *4* (5), 366−377.
(3) Service, R. F. *Science* **2011**, *332* (6037), 1494−1496.
(4) Obrovac, M. N.; Christensen, L. *Electrochem. Solid-State Lett.* **2004**, *7* (5), A93−A96.
(5) Chan, C. K.; Peng, H. L.; Liu, G.; McIlwrath, K.; Zhang, X. F.; Huggins, R. A.; Cui, Y. *Nat. Nanotechnol* **2008**, *3* (1), 31−35.
(6) Zhang, W. J. *J. Power Sources* **2011**, *196* (1), 13−24.
(7) Marom, R.; Amalraj, S. F.; Leifer, N.; Jacob, D.; Aurbach, D. *J. Mater. Chem.* **2011**, *21* (27), 9938−9954.
(8) Liu, X. H.; Zhang, L. Q.; Zhong, L.; Liu, Y.; Zheng, H.; Wang, J. W.; Cho, J.-H.; Dayeh, S. A.; Picraux, S. T.; Sullivan, J. P.; Mao, S. X.; Ye, Z. Z.; Huang, J. Y. *Nano Lett.* **2011**, *11* (6), 2251−2258.
(9) Beaulieu, L. Y.; Eberman, K. W.; Turner, R. L.; Krause, L. J.; Dahn, J. R. *Electrochem. Solid-State Lett.* **2001**, *4* (9), A137−A140.
(10) Cui, L. F.; Ruffo, R.; Chan, C. K.; Peng, H. L.; Cui, Y. *Nano Lett.* **2009**, *9* (1), 491−495.
(11) Magasinski, A.; Dixon, P.; Hertzberg, B.; Kvit, A.; Ayala, J.; Yushin, G. *Nat. Mater.* **2010**, *9* (4), 353−358.
(12) Scrosati, B.; Hassoun, J.; Sun, Y. K. *Energy Environ. Sci.* **2011**, *4* (9), 3287−3295.
(13) Goldman, J. L.; Long, B. R.; Gewirth, A. A.; Nuzzo, R. G. *Adv. Funct. Mater.* **2011**, *21* (13), 2412−2422.
(14) Bruce, P. G.; Scrosati, B.; Tarascon, J. M. *Angew. Chem., Int. Ed.* **2008**, *47* (16), 2930−2946.
(15) Park, M. H.; Kim, M. G.; Joo, J.; Kim, K.; Kim, J.; Ahn, S.; Cui, Y.; Cho, J. *Nano Lett.* **2009**, *9* (11), 3844−3847.
(16) Li, H.; Huang, X. J.; Chen, L. Q.; Wu, Z. G.; Liang, Y. *Electrochem. Solid-State Lett.* **1999**, *2* (11), 547−549.
(17) Hertzberg, B.; Alexeev, A.; Yushin, G. *J. Am. Chem. Soc.* **2010**, *132* (25), 8548−8549.
(18) Yao, Y.; McDowell, M. T.; Ryu, I.; Wu, H.; Liu, N.; Hu, L.; Nix, W. D.; Cui, Y. *Nano Lett.* **2011**, *11* (7), 2949−2954.
(19) Yamada, M.; Ueda, A.; Matsumoto, K.; Ohzuku, T. *J. Electrochem. Soc.* **2011**, *158* (4), A417−A421.
(20) Zhang, L. Q.; Liu, X. H.; Liu, Y.; Huang, S.; Zhu, T.; Gui, L.; Mao, S. X.; Ye, Z. Z.; Wang, C. M.; Sullivan, J. P.; Huang, J. Y. *ACS Nano* **2011**, *5* (6), 4800−4809.
(21) Cui, L. F.; Yang, Y.; Hsu, C. M.; Cui, Y. *Nano Lett.* **2009**, *9* (9), 3370−3374.
(22) Cui, L. F.; Hu, L. B.; Choi, J. W.; Cui, Y. *ACS Nano* **2010**, *4* (7), 3671−3678.
(23) Liu, X. H.; Zheng, H.; Zhong, L.; Huang, S.; Karki, K.; Zhang, L. Q.; Liu, Y.; Kushima, A.; Liang, W. T.; Wang, J. W.; Cho, J.-H.; Epstein, E.; Dayeh, S. A.; Picraux, S. T.; Zhu, T.; Li, J.; Sullivan, J. P.; Cumings, J.; Wang, C.; Mao, S. X.; Ye, Z. Z.; Zhang, S.; Huang, J. Y. *Nano Lett.* **2011**, *11* (8), 3312−3318.
(24) Lee, S. W.; McDowell, M. T.; Choi, J. W.; Cui, Y. *Nano Lett.* **2011**, *11* (7), 3034−3039.
(25) Liu, N.; Hu, L.; McDowell, M. T.; Jackson, A.; Cui, Y. *ACS Nano* **2011**, *5* (8), 6487−6493.
(26) Hu, L. B.; Wu, H.; Hong, S. S.; Cui, L. F.; McDonough, J. R.; Bohy, S.; Cui, Y. *Chem. Commun.* **2011**, *47* (1), 367−369.
(27) Newnham, R. E. *Properties of materials: anisotropy, symmetry, structure*; Oxford University Press: New York, 2005.
(28) Chon, M. J.; Sethuraman, V. A.; McCormick, A.; Srinivasan, V.; Guduru, P. R. *Phys. Rev. Lett.* **2011**, *107* (4), 045503.
(29) Kao, D. B.; McVittie, J. P.; Nix, W. D.; Saraswat, K. C. *IEEE Trans. Electron Devices* **1987**, *34* (5), 1008−1017.
(30) Mott, N. F.; Rigo, S.; Rochet, F.; Stoneham, A. M. *Philos. Mag. B* **1989**, *60* (2), 189−212.
(31) Seidel, H.; Csepregi, L.; Heuberger, A.; Baumgartel, H. *J. Electrochem. Soc.* **1990**, *137* (11), 3612−3626.
(32) Chan, M. K. Y.; Long, B. R.; Gewirth, A. A.; Greeley, J. P. *J. Phys. Chem. Lett.* **2011**, 3092−3095.
(33) Zhao, K. J.; Pharr, M.; Vlassak, J. J.; Suo, Z. G. *J. Appl. Phys.* **2011**, *109* (1), 016110.
(34) Huang, S.; Fan, F.; Liu, X. H.; Li, J.; Zhang, S.; Huang, J. Y.; Zhu, T. *J. Mech. Phys. Solids* **2011**, under review.
(35) Wortman, J. J.; Evans, R. A. *J. Appl. Phys.* **1965**, *36* (1), 153−156.
(36) Weirauch, D. F. *J. Appl. Phys.* **1975**, *46* (4), 1478−1483.
(37) Bean, K. E. *IEEE Trans. Electron Devices* **1978**, *25* (10), 1185−1193.
(38) Zhao, K.; Pharr, M.; Wan, Q.; Wang, W. L.; Kaxiras, E.; Vlassak, J. J.; Suo, Z. *J. Electrochem. Soc.* **2012**, *159* (3), A238−A243.
(39) Chen, L. Q. *Ann. Rev. Mater. Res.* **2002**, *32*, 113−140.
(40) Zhang, Q. F.; Zhang, W. X.; Wan, W. H.; Cui, Y.; Wang, E. G. *Nano Lett.* **2010**, *10* (9), 3243−3249.
(41) Sethuraman, V. A.; Chon, M. J.; Shimshak, M.; Srinivasan, V.; Guduru, P. R. *J. Power Sources* **2010**, *195* (15), 5062−5066.
(42) Shenoy, V. B.; Johari, P.; Qi, Y. *J. Power Sources* **2010**, *195* (19), 6825−6830.
(43) Zhao, K.; Wang, W. L.; Gregoire, J.; Pharr, M.; Suo, Z.; Vlassak, J. J.; Kaxiras, E. *Nano Lett.* **2011**, *11* (7), 2962−2967.
(44) Sethuraman, V. A.; Srinivasan, V.; Bower, A. F.; Guduru, P. R. *J. Electrochem. Soc.* **2010**, *157* (11), A1253−A1261.